Using confocal scanning laser microscopy for the in situ study of high-temperature behaviour of complex ceramic materials

Peter Tom Jones [*], David Desmet, Muxing Guo, Dirk Durinck, Frederik Verhaeghe,
Joris Van Dyck, Junhu Liu, Bart Blanpain, Patrick Wollants

Department of Metallurgy and Materials Engineering, Katholieke Universiteit Leuven, Kasteelpark Arenberg 44, BE-3001 Heverlee (Leuven), Belgium

Abstract

The confocal scanning laser microscopy (CSLM) technique has been successful in many metallurgical fields. This paper assesses its applicability to the in situ investigation of the high-temperature behaviour of complex ceramic materials. Magnesia–chromite refractory is selected as a ceramic test material. At room temperature, CSLM images correspond well to typical light optical microscopy (LOM) and backscattered electron (BSE) micrographs. In fact, because of the high axial resolution (short focal depth) and the confocal optics of the CSLM technique, the porosity level of the mirror polished ceramic specimens is more truthfully assessed by the CSLM (2-D) images than by the BSE micrographs (long focal depth). However, at high-temperatures (1550–1650 °C) the observed CSLM (2-D) image quality is slightly poorer. The principal explanation is the in situ roughening of the specimen surface during heating. The roughening has two causes: differential thermal expansion of the two primary phases in the ceramic test material and, to a lesser extent, thermal grooving. Nevertheless, it is shown that the CSLM image quality suffices for an in situ study of the high-temperature behaviour of ceramic materials. This is illustrated for the magnesia–chromite system by examining the dissolution mechanism of secondary (magnesiochromite) spinel into the periclase phase.
© 2007 Elsevier Ltd. All rights reserved.

Keywords: Electron microscopy; Thermal expansion; Spinels; Refractories; Confocal scanning laser microscopy

1. Introduction

By combining the advantages of a laser, confocal optics and an infrared image furnace (IIF), confocal scanning laser microscopy (CSLM) is a powerful technique that enables high-temperature in situ observation of a number of metallurgical phenomena.

Since the pioneering work of Emi and co-workers on real-time investigation of crystal growth and transformations in Fe–C alloys,[1,2] a multitude of successful studies have been performed. This includes the in situ observation of solidification and high-temperature phase transformations of steel and iron alloys,[3–5] the inclusion behaviour on liquid steel[6,7] and stainless steel[8] surfaces, the inclusion behaviour during steel solidification,[9–12] the inclusion behaviour at molten steel/slag interfaces,[13,14] the Marangoni flow at the solid/melt interface of steel,[15] the dissolu-tion of oxidic inclusions (or microparticles) in slags transparent to laser light,[16–22] and the crystallisation behaviour of slags.[23,24]

In the present work, it is assessed if the CSLM-IIF technique can also be applied to the investigation of the high-temperature behaviour of complex ceramic materials, such as refractories. To the best of the authors knowledge, this is the first study investigating the applicability of CSLM in this research field. Traditionally, high-temperature refractory behaviour is studied through post-mortem microstructural characterisation of worn specimens (either industrially worn or from laboratory furnace tests, e.g. Refs.[25–29]). Although this methodology has been quite successful, it is essentially an indirect technique where the his-tory of the sample has to be reconstructed from post-mortem analyses results. CSLM would, therefore, be an excellent com-plementary tool as it may provide direct, in situ information on complex solid state reaction mechanisms taking place at elevated process temperatures.

For the present feasibility study, a commercially available magnesia–chromite refractory type was selected as a ceramic test material. The reason for this choice is threefold. Firstly,

---

* Corresponding author. Tel.: +32 16 32 12 13; fax: +32 16 32 19 91.
  E-mail address: Peter.jones@mtm.kuleuven.be (P.T. Jones).

at high-temperatures the two principal phases in magnesia–chromite refractories (periclase and magnesiochromite spinel) strongly interact with one another, hence making this material an interesting case-study for in situ observations. Secondly, considerable knowledge on these materials has already been obtained by the present authors through post-mortem investigations[25–27,30]. Such studies may serve as a reference to compare the present CSLM observations. Finally, although environmental and economical restrictions motivate metallurgists to find chrome-free alternatives, for many demanding applications magnesia–chromite bricks remain the most suitable material currently commercially available. If the CSLM method proves to be successful for this complex ceramic material, then it can be extended to other ceramic systems.

2. Experimental methods and analysis

The experimental approach was to directly visualise the high-temperature behaviour of a complex refractory (ceramic) system with a CSLM. Particular zones in the refractory specimens were selected for thorough analysis. In order to allow for comparison, images were also obtained with light optical microscopy (LOM) and microprobe backscattered electron (BSE) images taken prior to and after the CSLM runs. Chemical and microstructural characterisation was performed with electron probe micro-analysis energy dispersive spectroscopy (EPMA-EDS). To evaluate the effect of high-temperature reactions between the distinct phases present in the system, roughness analyses were performed, also prior to and after the CSLM experiments.

2.1. CSLM

The experiments were performed with a confocal scanning laser microscope (Model 1LM21H, Lasertec) equipped with a high-temperature cell (Model SVF17SP, Lasertec). For a detailed description of the technique, we refer to the work of Emi and colleagues.[1,2] What follows here, is a summary of the CSLM essentials that are directly relevant for the present study. In the CSLM, He–Ne laser light (wavelength of 632.8 nm) is focussed by an objective lens onto the sample, with the reflected beam being focussed on a photon detector via a beam splitter. By scanning the focussed spot relative to the object an image can be constructed.

The CSLM technique operates with a confocal pinhole, which only permits light incident from the focal plane to pass through to the photon detector (Fig. 1). In contrast with conventional microscopy, in confocal optics the maximum intensity only occurs for the focussed points (Fig. 2). This implies that the axial resolution of the CSLM technique is high (i.e. short 'focal depth' or 'depth of field': ca. 0.2 μm for the ×100 objective lens with a numerical aperture (NA) of 0.95: supplier data). For smaller magnifications (e.g. ×20 objective lens) this focal depth is higher (see further). The pinhole also blocks the thermal radiation emitted from the specimen other than the focal plane. Hence, only the polarised reflection of the high intensity laser beam reaches the imaging sensor, thereby making it possible to observe samples at high lateral resolution (ca. 0.25 μm, for a
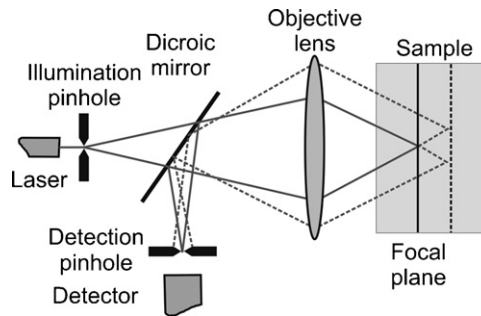

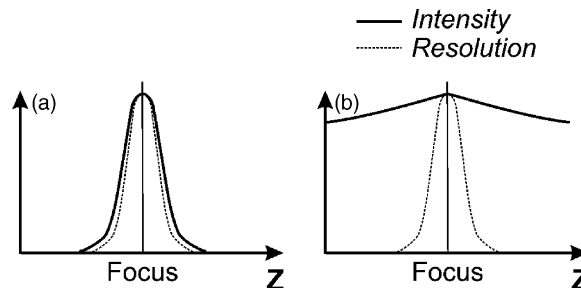Fig. 1. Principle of confocal optics used in CSLM [modified from Ref. [31]].

Fig. 2. Comparison between confocal (left) and conventional microscopy (right), with Z being the (vertical) distance from the objective lens.

×100 objective lens (NA = 0.95): supplier data) at elevated temperatures (theoretically up to 1700 °C with the present furnace setup).

Fig. 3 shows a schematic overview of the gold-plated paraboloid chamber (IIF), i.e. the high-temperature cell. The mirror polished refractory specimen (see further) is put into an alumina crucible (inner diameter = 5.9 mm, height = 4 mm), which in its turn is placed in a Pt sample holder equipped with a B-type thermocouple (PtRh). Fig. 4 shows the complete assembly, which is inserted in the hot zone of the high-temperature cell (upper focal point of the chamber). The heating occurs through
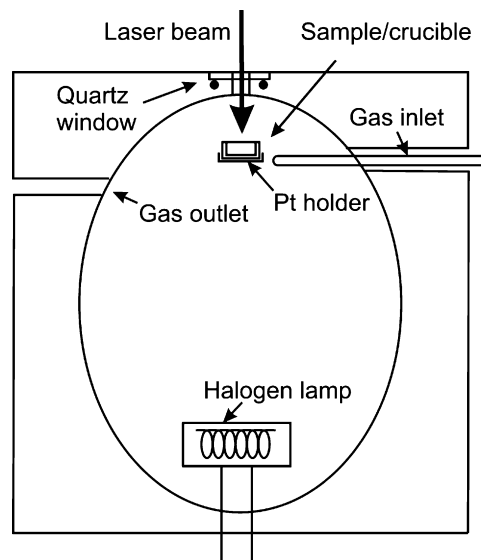

Fig. 3. Schematic of the high-temperature cell of the CSLM [modified from Ref. [14]].
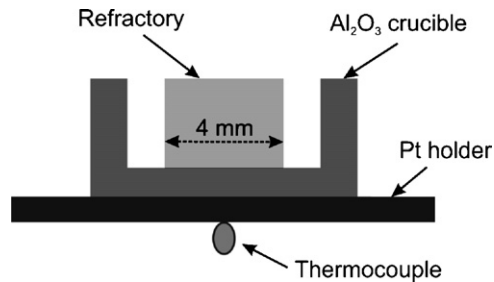
Fig. 4. A schematic of the sample and crucible configuration.

reflected light from the halogen bulb (1.5 kW), which is positioned in the lower focal point of the chamber. Prior to the actual CSLM refractory trials, the temperature was calibrated by the melting points of pure copper, nickel and cobalt. In the relevant temperature range, a (reproducible) temperature difference of $50 \pm 3\,^{\circ}C$ was observed between the measured temperature (thermocouple) and the sample temperature in the Al_2O_3 crucible. To achieve a sample temperature of, for instance, $1600\,^{\circ}C$, the set value for the PID-controller of the CSLM was programmed as $1650\,^{\circ}C$. The temperature difference is due to the heat transfer characteristics inside the IIF, as described in detail by Yin and Emi.[15]

2.2. Ceramic material and CSLM sample preparation

The investigated ceramic material was a commercially available rebonded magnesia–chromite refractory type (Ankrom S56, RHI Refractories), manufactured from presintered magnesia–chromite grains and large 'primary' chromite ore grains. The nominal composition (supplier data, in wt%) of the brick is 60% MgO, 18.5% Cr_2O_3, 13.5% FeO_x, 6% Al_2O_3, 1.3% CaO and 0.5% SiO_2, with a density of $3.38\,g/cm^3$ and an open porosity of 12 vol.%.

Smaller refractory specimens (e.g. ~3 mm height, 16 mm^2 base) were prepared for the CSLM runs as follows (Fig. 5). Typically, three to four refractory cylinders (4–7 mm height, 16 mm^2 base) were embedded in one sample using a high viscosity resin (Technovit), which was attached to a metal cylinder using double sided adhesive tape. This specimen was then ground (with Streurs P120, P320, P800 and P1200, representing SiC grain diameters of, respectively, 125, 46, 22 and 14 µm) until the thickness of the sample was approximately 3 mm. Subsequently, the
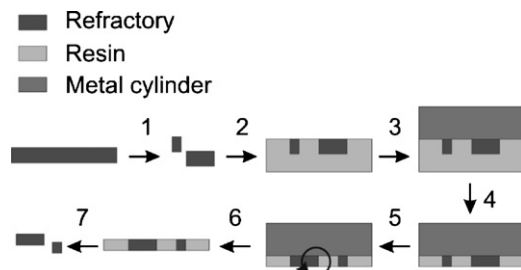

Fig. 5. Schematic overview of the CSLM sample preparation starting from a refractory cylinder and finishing with planparallel, mirror polished ceramic (refractory) specimens.

sample was polished using diamond suspensions (from Kemet) of 6, 3, 1 and, finally, 0.25 µm. The sample was then removed from the metal cylinder so that the other side could be ground and polished using the same procedure. Ultimately, the mirror polished sample was placed for 2 h into a recipient containing acetone in order to allow the dissolution of the resin. The procedure guarantees that samples are obtained that have plan parallel surfaces, which is of utmost importance to obtain a sound image quality.

2.3. Imaging and analysis techniques

Before the mirror polished refractory specimens were actually subjected to CSLM experiments, they were investigated by LOM and BSE imaging. To allow for a straightforward comparison between CSLM, BSE and LOM images, specific zones in the refractory sample were selected. For the BSE investigation, carbon was evaporated on the sample surface to provide a conducting layer for microscopical analysis. Before the CSLM experiment, this layer had to be carefully removed by 2 min of manual polishing with the 0.25 µm diamond suspension. After the CSLM experiments the same zones in the samples were reinvestigated with LOM and BSE imaging.

The BSE (compositional) micrographs were obtained with a JEOL JXA-733 Electron Probe Micro-Analysis system (thermionic electron gun, tungsten hairpin filament). The working conditions consisted of an accelerating voltage of 20 kV, a probe current of 2×10^{-8} A and a working distance of 11 mm. The BSE detector was a two-part annular-type semiconductor. A variation of atomic number within the specimen provides a variation in the amount of backscattered electrons (BSEs) produced during the interaction of the electron beam with the specimen, thus resulting in image 'Z-contrast'. BSE images are, therefore, well suited to provide information concerning the presence of phases. The higher the (average) atomic number of a refractory phase, the brighter that particular phase appears on a BSE micrograph.

The microprobe system was also used for EPMA-EDS analyses. This system is equipped with an energy dispersive spectroscopy system from Tracor Northern (5400 Series). The Semi-Quantitative (SQ) procedure from Tracor was used for quantitative elemental analysis. The SQ program requires that the operator selects a priori the oxides (e.g. FeO, Fe_2O_3) or elemental compounds (e.g. Fe) to be measured, as oxygen cannot be determined with the EDS Si(Li) detector (with Be window). Although in the analysed samples both FeO and Fe_2O_3 occur, for the sake of simplicity all FeO_x was determined as 'FeO'. Previous work has demonstrated that the present EPMA-EDS analysis procedure is sufficiently accurate and precise for the goals set in this work.[27,30]

LOM images were obtained prior to and after the CSLM experiments with a Metalloplan stereo light optical microscope from Leitz. Images were obtained with an objective lens of 80 (NA = 0.95), allowing a maximum magnification of ×950. The theoretical lateral resolution is 0.29 µm.

Roughness analyses were performed with a surface profilometer from WYKO NT3300 (from VEECO), which allows
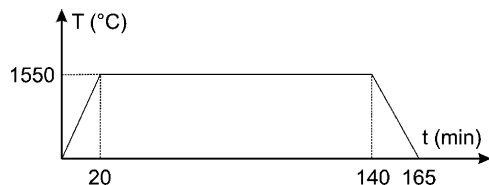
Fig. 6. Temperature profile during a CSLM test at 1550 °C.

to make scans to generate 2-D profiles and 3-D surface topographies. The analyses were performed in the vertical scanning interferometry (VSI) mode.

2.4. CSLM experiments

The CSLM runs were executed as follows. Before heating the refractory specimen, the high-temperature chamber was evacuated and flushed with argon. During the experiments an Ar stream was used continuously. Before entering the furnace this stream was passed through an oxygen scrubber (from Restek), which reduced the oxygen content to a value of approximately 20 ppb.

Samples were heated to the desired experimental temperature within approximately 20 min. Experiments were conducted at 1550, 1600 and 1650 °C (corresponding to set values in the CSLM of, respectively, 1600, 1650 and 1700 °C). These temperatures were maintained for 2 h, after which the specimens were cooled to room temperature in 25 min (Fig. 6). Considering the solid state of the specimen, this cooling rate was sufficiently rapid to freeze the high-temperature refractory state. The laser scanned images were recorded on video for further investigation. The procedure involved capturing and digitising images from the video, then reading the digitised images into a public domain image analysis software.[32]

3. Results and discussion

3.1. Characterisation as-delivered ceramic refractory material

Fig. 7 provides an overview image of the test material obtained through the combination of several BSE micrographs. The three specific regions that are highlighted in this image are reproduced at larger magnification in Fig. 8a–c. This ceramic material consists of periclase (magnesia), primary and secondary (magnesio)chromite $(Mg, Fe^{2+})[Cr, Al, Fe^{3+}]_2O_4$ spinel and a minor level of dicalciumsilicate ($2CaO \cdot SiO_2$ or C_2S) impurities. The latter cannot be seen in Fig. 8 since this phase is largely removed during sample preparation.[30]

The chromite is present as large crystals (i.e. primary chromite) and as secondary chromite (see Fig. 8a and b). Two types of secondary chromite can be distinguished. Type I is formed by intergranular precipitation during cooling and is located at periclase grain boundaries. Type II arises from intragranular exsolution precipitation from periclase grains on cooling, and thus forms within these periclase grains. Typical compositions for the distinct phases in this material are provided
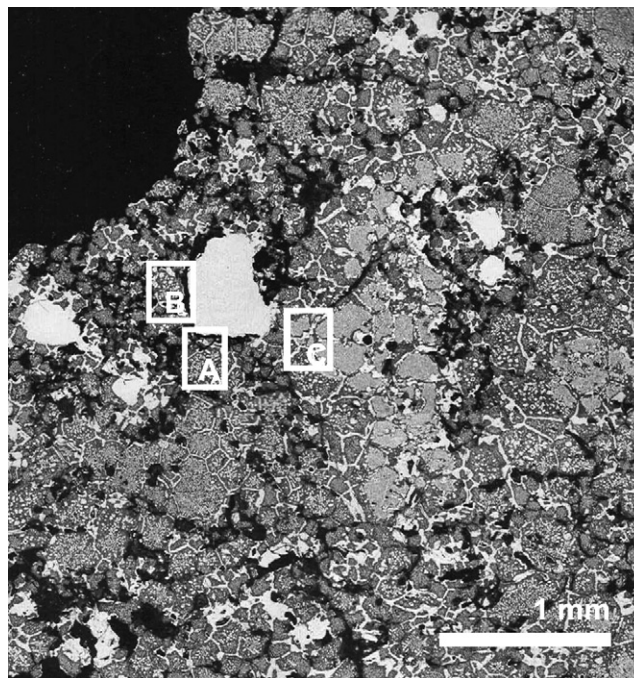

Fig. 7. BSE micrograph of the as-delivered magnesia–chromite refractory material. The highlighted zones A–C are shown in larger magnification in Fig. 8.

in Table 1. The as-delivered microstructure is characterised by a high proportion of direct bonding between the periclase matrix and the chromite, i.e. a direct attachment without any intermediate silicate film, as studied by Goto and Lee.[33] The intergranular secondary chromite is not only of great significance for the direct bonding but also for the protection against slag penetration when being applied in slagline areas of steelmaking or other linings.[27]

3.2. CSLM and LOM imaging at room temperature

Prior to the actual CSLM experiments, CSLM images were obtained at room temperature to determine the most suitable magnification range. The compromise between level of detail and image quality is highlighted in Fig. 9a–d, where room temperature CSLM images of magnesia–chromite refractory are shown for objective lenses (overall magnifications) of, respectively, 5 ($\times$350), 10 ($\times$700), 20 ($\times$1400) and 35 ($\times$2450). From this, it is concluded that the best images are obtained with an objective lens of 20, which corresponds to a magnification of $\times$1400. A striking feature of these figures is the large apparent porosity (depicted as black areas, see further).

3.2.1. Phase visualisation

For a more thorough comparison with LOM and CSLM images (respectively Fig. 10a and b) at room temperature, the zone shown in Fig. 8c was selected. From the LOM (objective lens $\times$80) and CSLM (objective lens $\times$20) images of this refractory zone, it can be concluded that they strongly resemble the BSE figures. The refractory phases (periclase and spinel) are depicted similarly, notwithstanding that the principle of CSLM/LOM optics is distinct from that of BSE imaging. In the former, the brightness of a phase is proportional to the
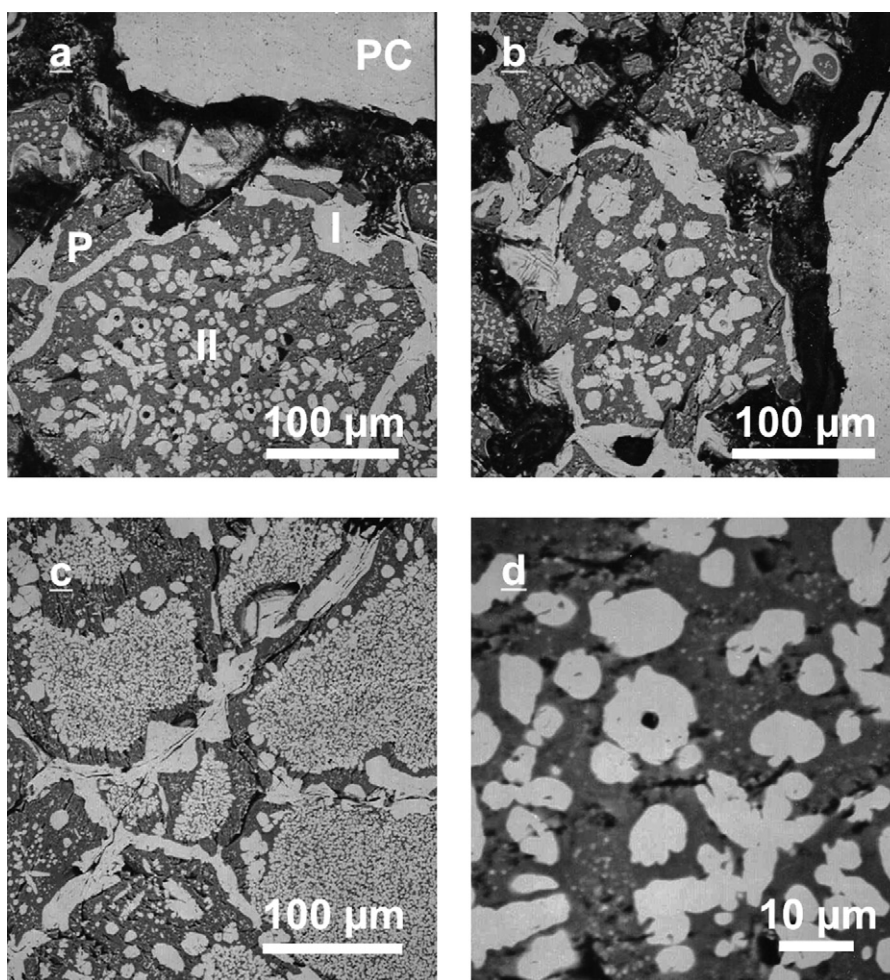
Fig. 8. BSE micrographs of (a–c) zones A–C in Fig. 7 (as-delivered magnesia–chromite refractory), (d) high magnification image of intragranular chromite [PC = primary chromite ore grain, P = periclase, I = intergranular secondary chromite spinel, II = intragranular secondary chromite spinel].

level of reflected light, whereas in the latter it is based on the number of backscattered electrons produced. This BSE yield is dependent on the (weighted) average atomic number ($\bar{Z}$) of a phase, explaining why in BSE micrographs magnesiochromite spinel ($\bar{Z}_{MgCr_2O_4} = 17.15$) appears brighter than periclase ($\bar{Z}_{MgO} = 10.41$). Due to this large $\bar{Z}$-contrast, the BSE imaging is an excellent method to visualise the different phases in magnesia–chromite refractory systems. Note that in the case of magnesia–$MgAl_2O_4$ spinel bricks the $\bar{Z}$-contrast is more limited, which results in less contrast in the BSE mode

($\bar{Z}_{MgAl_2O_4} = 10.57$). The effectivity of BSE imaging, hence, also depends on the ceramic material.

3.2.2. Porosity level

Although the CSLM/LOM figures of the investigated material strongly resemble the BSE micrographs, there is one major difference. The LOM and especially the CSLM images reveal a higher porosity level with reference to the BSE micrographs. This is mainly due to the fact that the focal depths (and the axial resolutions) of these techniques are very different. In micro-

Table 1

Composition and standard deviations of the magnesia–chromite refractory phases for the as-delivered condition and the situation at 1600 °C (JEOL 733) (reproduced from Ref. [27])

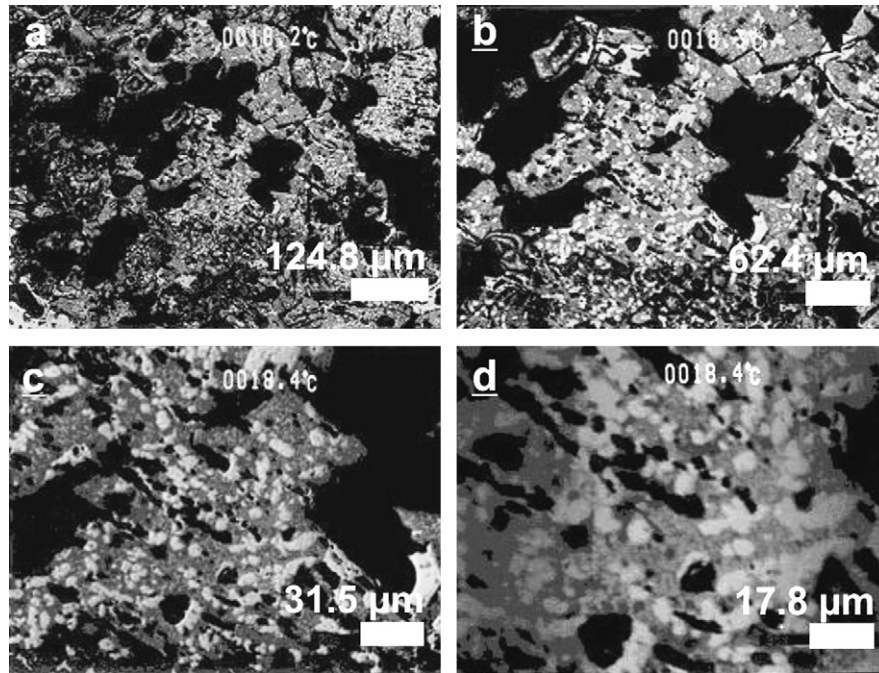| Phase	State	MgO (wt%)	CaO (wt%)	SiO$_2$ (wt%)	Al$_2$O$_3$ (wt%)	Cr$_2$O$_3$ (wt%)	FeO[a] (wt%)
Periclase	As-delivered	95 ± 1	<0.5	<0.5	<1	1.9 ± 1.1	1.7 ± 1.2
	At 1600°C	69 ± 3	<1	<0.5	3.5 ± 0.6	13 ± 1	13 ± 1
Secondary chromite	As-delivered	21 ± 2	0.5 ± 0.1	<0.5	15.1 ± 0.2	42 ± 1	20 ± 2
	At 1600 °C	21 ± 2	0.6 ± 0.3	<0.5	15.1 ± 0.6	44 ± 1	19 ± 1
Primary chromite	As-delivered	18.3 ± 0.6	1.0 ± 0.7	<1	15.9 ± 0.3	52 ± 2	11 ± 1
	At 1600 °C	18.6 ± 0.5	0.4 ± 0.1	<0.5	15.7 ± 0.7	53 ± 1	12 ± 1

[a] All iron oxide inside the brick was expressed as 'FeO'.

Fig. 9. Room temperature CSLM images of the as-delivered magnesia–chromite refractory for objective lenses of (a) ×5, (b) ×10, (c) ×20 and (d) ×35.

probe imaging, focal depths are large because of the small electron beam divergence angle (α), as defined by the semi-cone angle. The following quantitative data can be obtained for the present microprobe setup. For a final aperture radius of 85 μm (R) and a working distance (WD) of 11 mm, α is 7.7×10^{-3} rad ($\alpha = R \times \mathrm{WD}^{-1}$). If one considers that defocusing becomes objectionable when the beam size overlaps two picture elements (of a size 0.1 mm on the cathode ray tube), the depth of field (D) can then be found as:

$$D_{\mathrm{microprobe}} = \frac{0.2\,\mathrm{mm}}{\alpha \times M} \tag{1}$$

with M being the magnification.[34] For microprobe BSE images obtained at magnifications of ×300 (see e.g. Fig. 8a) and ×1600 (e.g. Fig. 8d), this results in focal depths of, respectively, 86.5 and 16.2 μm. For a magnification of 1400 (cf. CSLM overall magnification) this leads to a depth of field of 18.5 μm.

In LOM and CSLM imaging the focal depth is much shallower, which is due to the fact that the divergence angle (α) of the objective lens is much larger. Using wave theory and objective measurements made with a variety of lenses and wavelengths, Young et al.[35] proposed the following formula for the focal depth of a microscope system:

$$D_{\mathrm{microscope}} = \frac{\lambda}{4n(1 - \sqrt{1 - (\mathrm{NA}/n)^2})} \tag{2}$$

where λ is the wavelength of the used light, n the index of refraction and NA is the numerical aperture of the objective lens. For the used CSLM setup ($n = 1$, $\lambda = 632.8$ nm, objective lens of ×20 with NA $= 0.35$ and an overall magnification ×1400), this leads to a depth of field of 2.5 μm (D_{CSLM}). This value may be compared with the microprobe focal depth at the same magnification ($D_{\mathrm{microprobe}} = 18.5\,\mu$m).

This difference in focal depth has important repercussions for how pores are depicted in refractory imaging, which is schematically illustrated in Fig. 11. Consider a superficial pore at the refractory surface ($\sim$5 μm deep) with periclase in the immediate vicinity (both under and next to the pore). Taking into account the large depth of field for a BSE image, the pore/periclase boundary will appear in focus (Fig. 11a). Concurrently, backscattered electrons originating from the periclase in the vicinity of the boundary will contribute to a periclase compositional signal in the BSE micrograph. The superficial pore will not be visible on the image; if it is deeper and/or wider it will only be partially represented on the BSE micrograph. Hence, in BSE microprobe imaging the actual porosity level (open porosity = 12 vol.%, supplier data) tends to be underestimated. Now reconsider the superficial pore in the refractory surface during CSLM (LOM) imaging. Because of the shallow focal depth, the main part of the pore/periclase boundary will be out of focus (Fig. 11b). In the case of CSLM imaging, there is the additional element of confocal optics. In the present application, the focal plane is the surface of the (ceramic) refractory specimen (which is not transparant to laser light). Only the information present in this confocal plane is used for 2-D image construction; all the rest is filtered. Therefore, the superficial pore in the refractory surface will be straightforwardly depicted as a black spot. Hence, in CSLM images the observed porosity level will be closer to the actual porosity.

3.2.3. CSLM 3-D images

In this context, it should be pointed out that by scanning a surface at various focal depths, 3-D CSLM images of uneven samples with dents and pimples can be constructed.[1] However, in the present study the goal is to make an in situ investigation of the high-temperature behaviour of a complex ceramic material.
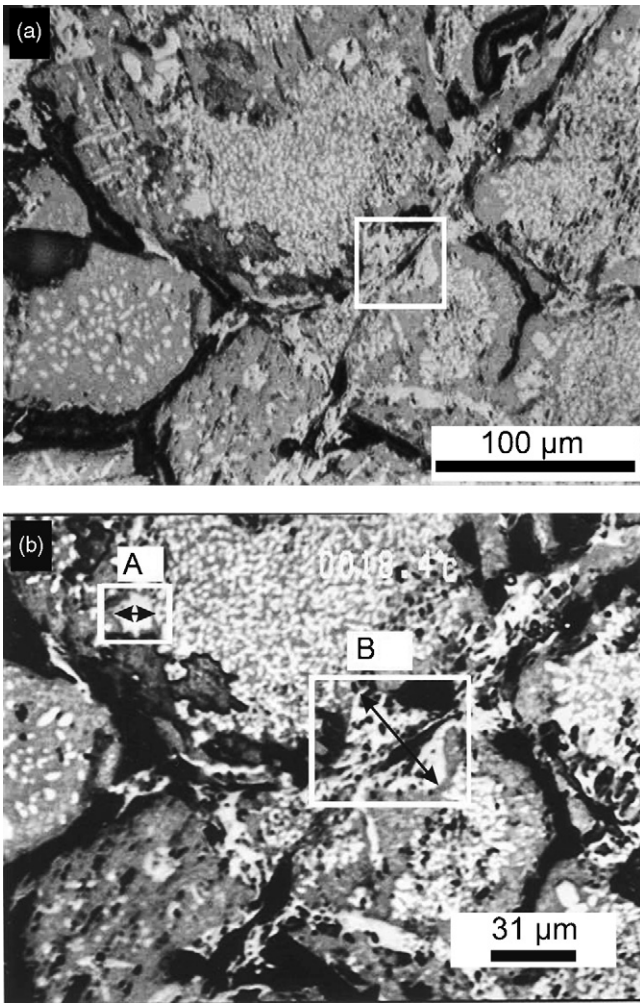
Fig. 10. Room temperature images of the as-delivered magnesia–chromite refractory using (a) LOM and (b) CSLM (objective lens ×20).
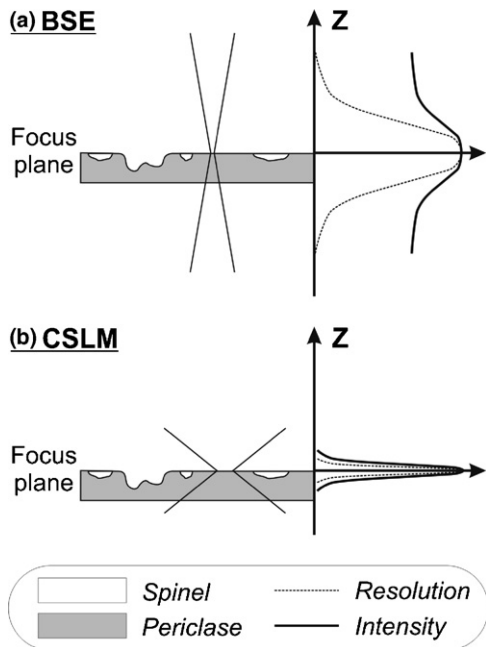

Fig. 11. Qualitative comparison between microprobe BSE imaging and CSLM imaging at room temperature, with reference to how a superficial pore is depicted.

This requires a continuous focusing on the focal plane, being the (initially) mirror polished refractory surface. It is thus not possible to simultaneously produce 3-D images and follow up high-temperature chemical interactions in situ.

3.3. High-temperature imaging

The previous section highlighted that, provided the samples are plan parallel and mirror polished, the CSLM (2-D) image quality at room temperature is good for the present ceramic refractory material. This section investigates the CSLM image quality at temperatures relevant to steelmaking. Refractory samples were heated in the CSLM system to temperatures between 1550 and 1650 °C. In order to obtain sharper images, the thermal expansion of the refractory specimens had to be counteracted by shifting the (vertical) Z-axis of the CSLM equipment so that the refractory surface corresponded to the CSLM focal plane. Fig. 12a and b present CSLM images at 1550 °C after 2240 and 8000 s (respectively, ~37 and 133 min). When comparing Fig. 12 with the room temperature CSLM images (Fig. 10b) a minor loss in sharpness can be observed. It is believed that this image quality loss is, apart from some unavoidable thermal radi-
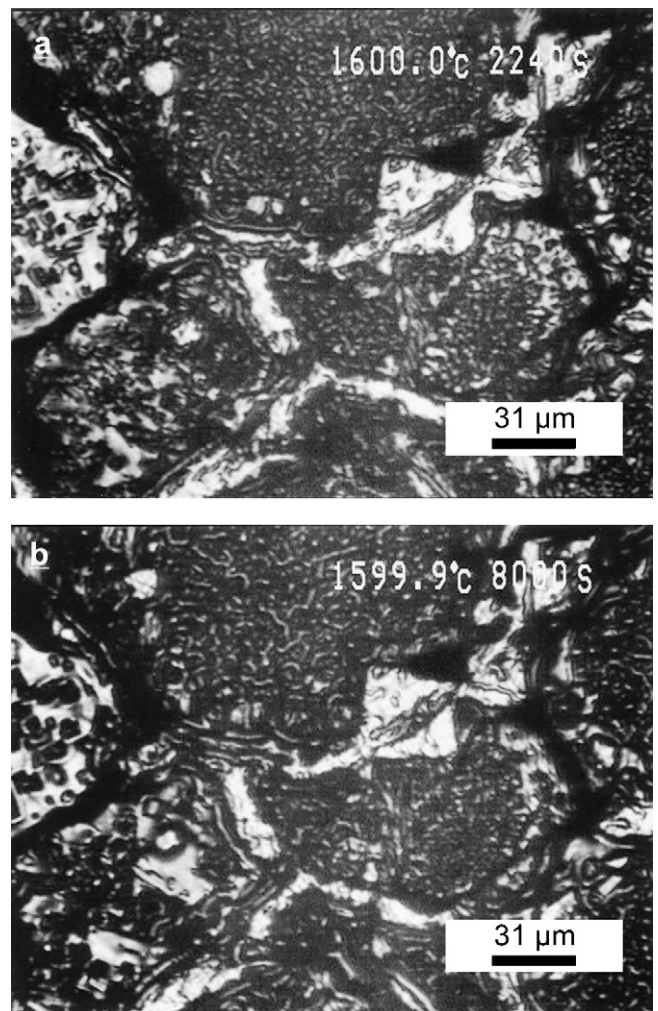

Fig. 12. Magnesia–chromite CSLM images at 1550 °C (i.e. sample temperature) after (a) 2240 s and (b) 8000 s.
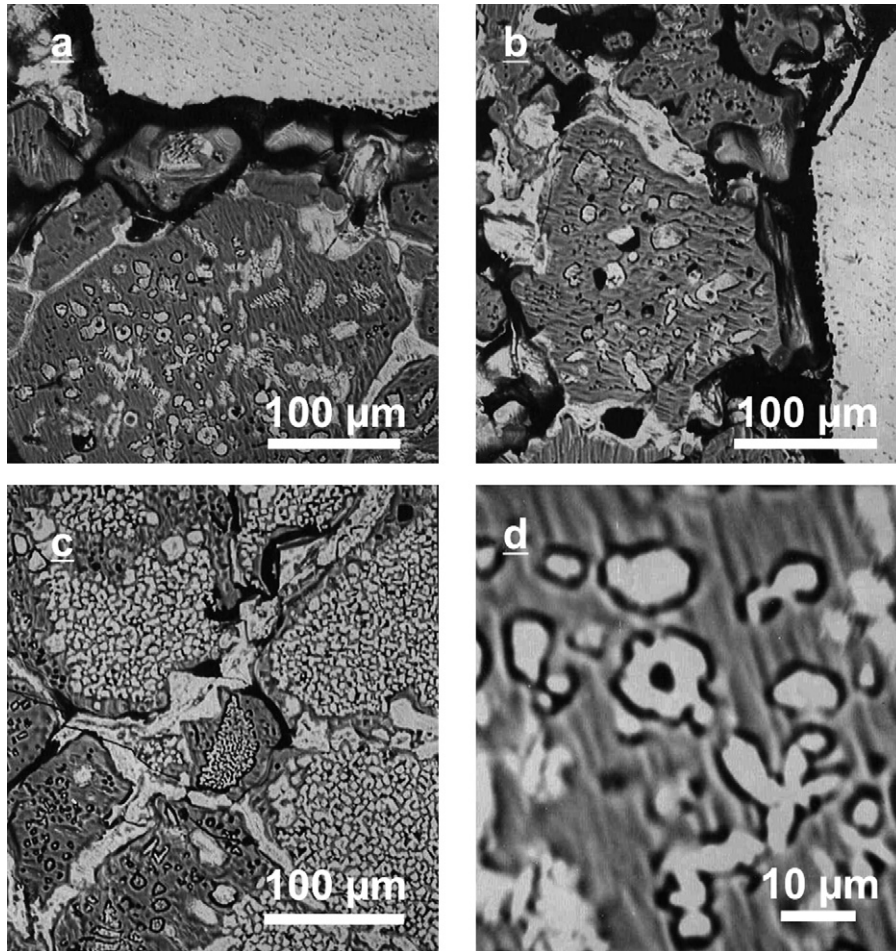
Fig. 13. Post-CSLM (1550 °C, 2 h) BSE micrographs of (a–c) zones A–C in Fig. 7 (as-delivered magnesia–chromite refractory), (d) high magnification image of the highlighted zone in Fig. 8a.

ation originating from the focal plane, predominantly related to intrinsic modifications in the refractory specimen, independently from the CSLM optics.

To find evidence for this hypothesis, the rapidly cooled CSLM specimens were investigated with BSE and LOM imaging. In order to assess the real state of these samples, they were directly analysed without any grinding/polishing after the CSLM runs. In the case of EPMA-EDS analysis, a carbon layer was deposited. Fig. 13a–d presents BSE images of the post-CSLM microstructure. For the sake of comparison, the same zones as in Fig. 8 (prior to CSLM) are presented. In Fig. 14b, a LOM image is provided of the area shown in Fig. 13c (and Fig. 8c).

These images confirm that upon heating the sample itself undergoes fundamental changes. The image sharpness of the high-temperature and rapidly cooled samples – as obtained by BSE and LOM – is lower with respect to the initial mirror polished specimens. This becomes clear when comparing the highest magnification BSE micrographs prior to (Fig. 8d) and after (Fig. 13d) the CSLM experiment. The initially mirror polished surface has roughened, leading to poorer image sharpness in the CSLM (short focal depth). The reasons for surface roughening are two-fold: differential thermal expansion and thermal grooving.

3.3.1. Differential thermal expansion

The first and predominant cause of roughening is due to the difference in thermal expansion coefficients of magnesia and spinel, the two principal refractory phases. Estimations of these coefficients are, respectively, $13.6 \times 10^{-6}\,°C^{-1}$ (from 25 to 1000 °C, i.e. for MgO) and $8.4 \times 10^{-6}\,°C^{-1}$ (from 25 to 1000 °C, i.e. for natural $MgAl_2O_4$ spinel).[36] During the experiment, periclase thus expands more strongly than chromite spinel. At the surface, the chromite is being pushed out of the original plane.

This was confirmed by roughness analyses. Firstly, it was corroborated that the CSLM sample preparation did indeed produce perfectly polished surfaces. Fig. 14a presents a CSLM image of a typical (polished) magnesia–chromite specimen prior to the heating procedure. The two highlighted zones correspond to the pores in the surface. Fig. 14b presents a 2-D profilometer scan of this sample, showing that the initial smoothness of the surface was very good: the height difference between chromite and periclase was $0.2\,\mu m$ maximum, which is smaller than the CSLM focal depth for the present conditions ($D_{CSLM} = 2.5\,\mu m$ when NA is 0.35). The situation after completion of the CSLM runs is completely different. A 2-D surface scan, corresponding with Fig. 14c (and Fig. 13c), is depicted in Fig. 14d. In this case,
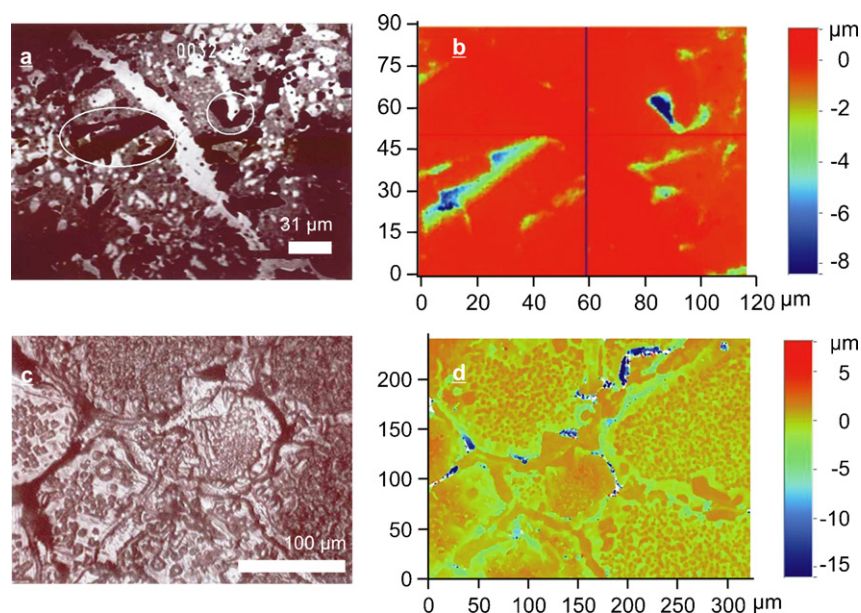
Fig. 14. (a) Room temperature CSLM image of a typical mirror polished magnesia–chromite sample surface and (b) a 2-D profilometer surface scan of this region; and (c) post-CSLM (1550 °C, 2 h) LOM image of the same zone depicted in Fig. 12c and (d) a 2-D profilometer surface scan of this zone.

height differences are found in the order of magnitude of 5 μm, with the chromite phase being situated higher than the periclase. This value is substantially different from the initial roughness level and, furthermore, exceeds D_{CSLM}, corroborating that the loss of imaging sharpness in high-temperature CSLM imaging is essentially caused by differential thermal expansion.

3.3.2. Thermal grooving

A concurrent feature that becomes apparent from the BSE images taken after completion of the experiment is the occurrence of dark (and thus porous) ridges around the intragranular secondary chromite grains (Fig. 13d). These dark rims are due to a phenomenon that resembles the mechanism of thermal grooving. The latter has been well documented by Dippenaar and Phelan[5] in low-carbon steels. Where grain boundaries intersect the free surface, the need for energy minimisation results in the formation of a V-shaped groove. This occurs through the surface diffusion of atoms. In the application of thermal etching, the phenomenon of thermal grooving is desired as this allows the visualisation of grain boundaries. It has been shown that thermal etching is, for example, a very adequate method for revealing austenite grain boundaries in carbon steels.[37] LOM can then be used. Similarly, during high-temperature CSLM imaging, the existence of such grooves alters the optical path of the reflected light. Some reflected rays are scattered, leading to the development of contrast.[5] In the present case, where two chemically interacting and differentially expanding phases are present, the situation is more complex. The principle of energy minimisation at the triple junction between the phase boundary (periclase/spinel) and the free surface is, nevertheless, also valid here. Hence, similar grooves will be formed through surface diffusion. This phenomenon is, however, superimposed on (1) the previously discussed mechanism of surface roughening through differential expansion and (2) the diffusion of atoms due to the high-temperature dissolution of intragranular chromite in

the surrounding periclase solid solution (see next paragraph). The 'thermal grooving' phenomenon observed in these samples is believed to have two different effects. On the one hand, it will accentuate the magnesia/spinel phase boundaries, leading to a better visualisation of the boundary between the two phases. On the other hand it will lead to an additional roughening of the sample surface, thereby slightly compromising the image sharpness. As discussed in the previous section, this is due to the confocal optics and the short focal depth of the CSLM. Nevertheless, as will be shown in the next paragraph, the CSLM image quality (Fig. 12) suffices for the in situ investigation of key high-temperature interaction mechanisms in ceramics.

3.4. In situ study of spinel dissolution

One particularly relevant phenomenon for magnesia–chromite refractory materials, is the gradual dissolution of chromite spinel into the periclase solid solution at sufficiently high-temperatures. In industrial practice this is quite important as the advantage, with respect to slag penetration, of having a two-phase refractory system (periclase + spinel) is gradually lost at elevated temperatures. This is due to the process that the present authors[27] designated as 'inactivation of secondary chromite'. The phenomenon refers to the transformation of a two-phase system (periclase + spinel) into a one-phase system (periclase solid solution), which is prone to strong slag infiltration along the periclase grain boundaries. The present authors studied this phenomenon at temperatures up to 1800 °C using a hybrid microwave heating furnace. Samples were quenched and studied using post-mortem EPMA-EDS and SEM investigations. It was shown that at elevated temperatures the chromite spinel components dissolve into a (Mg, Cr, Fe, Al)O periclase solid solution. EPMA-EDS analyses have found typical compositions for the high-temperature periclase (in wt%) of 73% MgO, 2.7% Al_2O_3, 13.8% FeO and 9.9% Cr_2O_3 (quenched after 2 h

Table 2
Change in dimension (in μm) of two secondary chromite grains (depicted as 'A' and 'B' in Fig. 10b), measured at room temperature and during a CSLM test at 1550 °C

Grain	Fig. 10b (room temperature)	Fig. 11a (1550 °C, 2240 s)	Fig. 11b (1550 °C, 8000 s)
A	13.5	11.4	11.1
B	44.4	43.3	42.5

at 1600 °C, Table 1), which should be compared with the purity of the periclase in the as-delivered structure: 95% MgO, <1% Al_2O_3, 1.7% FeO and 1.9% Cr_2O_3 (Table 1).

The CSLM experiments allow us to investigate the dissolution mechanism of spinel into periclase in situ, as a function of time and temperature. As a first indication for this dissolution, the reduction in diameter of two secondary spinel fragments (zones A and B in Fig. 10b) was quantified (Table 2). Once it was established that the present procedure was able to monitor this mechanism, a more systematic study was performed. For a range of temperatures, magnesia–chromite samples were heated and kept at the required temperature for 2 h. CSLM images were generated prior and during the experiment (every 2 min). Specific areas were preselected and investigated. Fig. 15 compares the

Fig. 15. CSLM image of a periclase grain containing intragranular chromite grains (a) prior to a CSLM test and (b) after a CSLM run (1600 °C, 2 h).
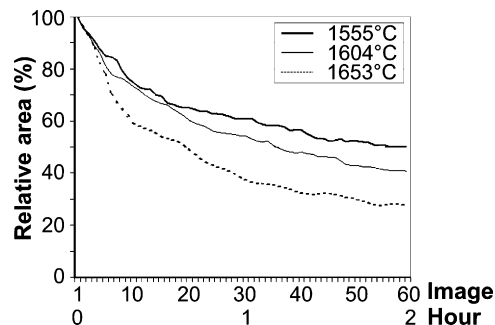

Fig. 16. Dissolution of intragranular secondary chromite spinel in periclase solid solution with time and temperature, as in situ observed in the CSLM.

situation prior to the CSLM experiment and after 2 h at 1600 °C. By measuring and averaging (relative to initial size) the dissolution process of 10 intragranular spinel grains (within a range of 10–20 μm) into the surrounding periclase matrix, and using the image software analysis the relative surface spinel area as a function of time and temperature was plotted. Fig. 16 reveals that the dissolution rate is highest during the initial ten minutes of the experiments and is, furthermore, proportional to temperature. These results thus allow for the determination of the thermodynamics (dissolution potential of spinel components into the periclase solid solution) and kinetics (diffusion versus reaction controlled?) of this process. A detailed description is given in a separate paper by the present authors[38] where the CSLM results are compared with other laboratory studies of this material (in bottom loading and hybrid microwave furnaces) and theoretical dissolution models.

4. Conclusions

The CSLM-IIF technique has proven to be a successful method in a number of metallurgical fields. In the present paper, an assessment was made of its applicability for the in situ investigation of the high-temperature behaviour of complex ceramics. Magnesia–chromite refractory was selected as the test material. At room temperature, with respect to phase visualisation, CSLM images corresponded well to typical BSE micrographs. In fact, because of the short focal depth and the confocal optics of the CSLM, the porosity level of the ceramic material was more truthfully assessed by the CSLM (2-D) images than by the BSE micrographs (long focal depth), provided that the samples were plan parallel and mirror polished.

At high-temperatures (1550–1650 °C) the observed CSLM image quality was slightly poorer than at room temperature. This can mainly be explained by the in situ roughening of the specimen surface during heating, which compromised the CSLM
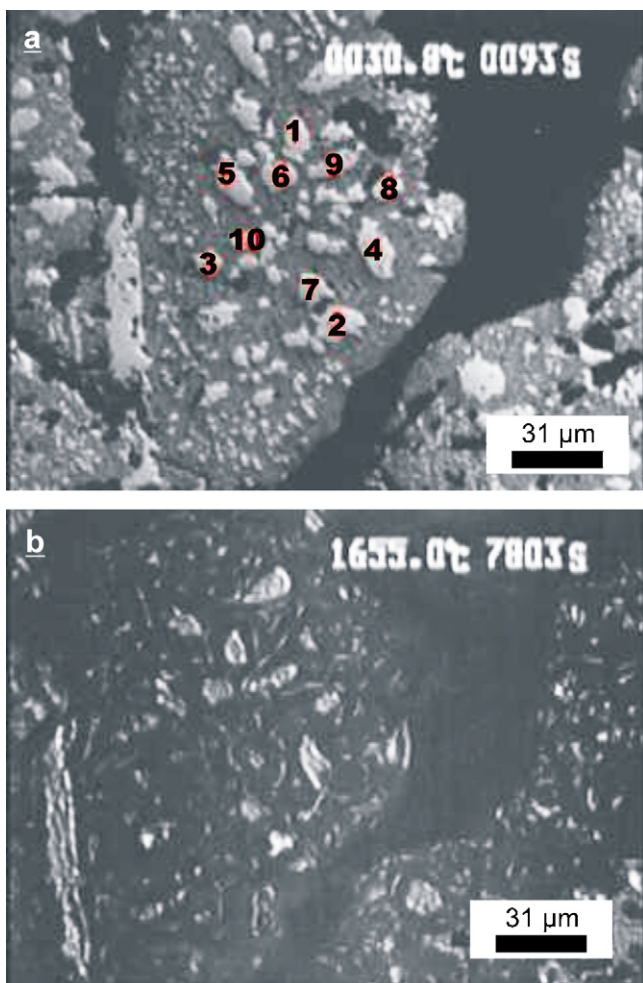
2-D image quality (short focal depth and confocal optics). The roughening has two causes: differential thermal expansion of the two primary phases in the ceramic test material and, to a lesser extent, thermal grooving.

Nevertheless, it was shown that the CSLM 2-D image quality at elevated temperatures (up to $1650\,^{\circ}$C) suffices in order to in situ study the high-temperature behaviour of complex ceramic materials. This was illustrated for the magnesia–chromite system by examining the dissolution mechanism of secondary spinel into the periclase phase. From this, it may be concluded that, despite some limitations, the CSLM-IIF technique is applicable to the direct observation of high-temperature phenomena in complex ceramic materials.

References

1. Chikama, H., Shibata, H., Emi, T. and Suzuki, M., In situ real time observation of planar to cellular and cellular to dendritic transition of crystals growing in Fe–C alloy melts. *Mater. T. JIM*, 1996, **37**(4), 620–626.
2. Yin, H., Emi, T. and Shibata, H., Determination of free energy of Δ-ferrite/Γ-austenite interphase boundary of low carbon steels by in situ observation. *ISIJ Int.*, 1998, **38**(8), 794–801.
3. Phelan, D., Stanford, N. and Dippenaar, R., In situ observations of Widmanstätten ferrite formation in a low-carbon steel. *Mater. Sci. Eng. A*, 2005, **407**, 127–134.
4. Phelan, D., Reid, M., Dippenaar, R. and Experimental, Modelling studies into high temperature phase transformations. *Comp. Mater. Sci.*, 2005, **34**, 282–289.
5. Dippenaar, R. and Phelan, D. J., Delta-ferrite recovery structures in low-carbon steels. *Metall. Trans. B*, 2003, **34B**, 495–501.
6. Yin, H., Shibata, H., Emi, T. and Suzuki, M., In situ observation of collision agglomeration and cluster formation of alumina inclusion particles on steel melts. *ISIJ Int.*, 1997, **37**(10), 936–945.
7. Yin, H., Shibata, H., Emi, T. and Suzuki, M., Characteristics of agglomeration of various inclusions particles on molten steel surface. *ISIJ Int.*, 1997, **37**(10), 946–955.
8. Luo, H., Interaction between inclusion particles on the stainless-steel melt surface. *Scand. J. Metall.*, 2001, **30**, 212–219.
9. Shibata, H., Yin, H., Yoshinaga, S., Emi, T. and Suzuki, M., In situ observation of engulfment and pushing of nonmetallic inclusions in steel melt by advancing melt/solid interface. *ISIJ Int.*, 1998, **38**(2), 149–156.
10. Wang, Y., Valdez, M. and Sridhar, S., Liquid, solid, inclusions at advancing steel solidification fronts. *Z. Metallkd.*, 2002, **93**(1), 12–20.
11. Wang, Y. and Sridhar, S., The behavior of Al_2O_3–CaO inclusions in low-carbon Al-killed steel. In *2002 Electric Furnace Conference Proceedings*, 2002, pp. 275–285.
12. Wang, Y., Valdez, M. and Sridhar, S., Formation of CaS on Al_2O_3–CaO inclusions during solidification of steels. *Metall. Trans. B*, 2002, **33B**, 625–632.
13. Coletti, B., Vantilt, S., Blanpain, B. and Sridhar, S., Observation of calcium aluminate inclusions at interfaces between Ca-treated Al-killed steels and slags. *Metall. Trans. B*, 2003, **34B**, 533–538.
14. Shannon, G., Wang, Y., Vantilt, S., Coletti, B., Blanpain, B. and Sridhar, S., Observations of behaviour of oxide inclusions at molten slag/steel interfaces. In *VII International Conference on Molten Slags, Fluxes and Salts*, 2004, pp. 571–576.
15. Yin, H. B. and Emi, T., Marangoni flow at the gas/melt interface of steel. *Metall. Trans. B*, 2003, **34**(5), 483–493.
16. Liu, J., Guo, M., Jones, P. T., Blanpain, B. and Wollants, P., In-situ observation of MgO dissolution in calcia-alumina-silicate based slags. *J. Eur. Ceram. Soc.*, 2007, **27**, 1961–1972.
17. Yi, K. W., Tse, C., Park, J.-H., Valdez, M., Cramb, A. W. and Sridhar, S., Determination of dissolution time of Al_2O_3 and MgO inclusions in synthetic Al_2O_3–CaO–MgO slags. *Scand. J. Metall.*, 2003, **32**, 177–184.
18. Sridhar, S. C. and Cramb, A. W., Kinetics of Al_2O_3 dissolution in CaO–MgO–SiO_2–Al_2O_3 slags: in situ observations and analysis. *Metall. Trans. B*, 2000, **31B**, 406–410.
19. Valdez, M., Prapakorn, K., Cramb, A. W. and Seetharaman, S., A study of the dissolution of Al_2O_3 MgO and $MgAl_2O_4$ particles in a CaO–Al_2O_3–SiO_2. *Slag. Steel Res.*, 2001, **72**(8), 291–297.
20. Valdez, M., Prapakorn, K., Sridhar, S. and Cramb, A. W., Dissolution of inclusions in steelmaking slags. In *ISSTech 2003 Conference*, 2003, pp. 789–798.
21. Monaghan, B. J., Nightingale, S. A., Chen, L. and Brooks, G. A., The dissolution behavior of selected oxides in CaO–SiO_2–Al_2O_3 slags. In *VII International Conference on Molten Slags and Salts*, 2004, pp. 585–594.
22. Tse, C., Lee, S. H., Sridhar, S. and Cramb, A. W., In situ observations relevant to clean steel: dissolution of alumina particles in slags. In *2000 Steelmaking Conference Proceedings*, 2000, pp. 219–229.
23. Orrling, C., Fang, Y., Phinichka, N., Sridhar, S. and Cramb, A. W., Observing and measuring solidification phenomena at high temperatures. *JOM-e*, 1999, **51**(7).
24. Orrling, C., Sridhar, S. and Cramb, A. W., In situ observation of the role of alumina particles on the crystallization behavior of slags. *ISIJ Int.*, 2000, **40**(9), 877–885.
25. Jones, P. T., Blanpain, B., Wollants, P., Hallemans, B., Heylen, G. and Weytjens, J., Extending the lining life of Alz Nv's Ladle lining. *Iron Steelmak.*, 1999, **26**(12), 31–35.
26. Jones, P. T., Blanpain, B., Wollants, P., Ding, R. and Hallemans, B., Degradation mechanisms of magnesia–chromite refractories in vacuum-oxygen decarburisation ladles during production of stainless steel. *Ironmak. Steelmak.*, 2000, **27**(3), 228–237.
27. Jones, P. T., Vleugels, J., Volders, I., Blanpain, B., Van Der Biest, O. and Wollants, P., A study of slag-infiltrated magnesia–chromite refractories using hybrid microwave heating. *J. Eur. Ceram. Soc.*, 2002, **22**, 903–916.
28. Goto, K., Argent, B. B. and Lee, W. E., Corrosion of MgO–Al_2O_4 spinel refractory bricks by calcium aluminosilicate slag. *J. Am. Ceram. Soc.*, 1997, **80**(2), 461–471.
29. Guo, M., Jones, P. T., Parada, S., Boydens, E., Van Dyck, J., Blanpain, B. *et al.*, Degradation mechanisms of magnesia–chromite refractories by high-alumina stainless steel slags under vacuum conditions. *J. Eur. Ceram. Soc.*, 2006, **26**, 3831–3843.
30. Jones, P. T., *Degradation Mechanisms of Basic Refractory Materials During the Secondary Refining of Stainless Steel in VOD Ladles*. K.U. Leuven, Leuven, 2001.
31. van de Velde, F., Weinbreck, F., Edelman, M. W., van der Linden, E. and Tromp, R. H., Visualisation of biopolymer mixtures using confocal scanning laser microscopy (CSLM) and covalent labelling techniques. *Colloid Surface B*, 2003, **31**, 159–168.
32. NIH Image (Version 1.62), developed at U.S. National Institute of Health.
33. Goto, K. and Lee, W. E., The direct bond in magnesia chromite and magnesia spinel refractories. *J. Am. Ceram. Soc.*, 1995, **78**(7), 1753–1760.
34. Goldstein, J. I., Newbury, D. E., Echlin, P., Joy, D. C, Fiori, C. and Lifshin, E., *Scanning Electron Microscopy and X-ray Microanalysis*. Plenum Press, New York, 1981.
35. Young, I. T., Zagers, R., van Vliet, L. J., Mullikin, J., Boddeke, F. and Netten, H., Depth-of-focus in microscopy. In *8th Scandinavian Conference on Image Analysis*, 1993, pp. 493–498.
36. Cemail, A. and Riley, F. L., Effect of the particle size distribution of spinel on the mechanical properties and thermal shock performance of MgO–spinel composites. *J. Eur. Ceram. Soc.*, 2003, **23**, 3079–3087.
37. García de Andrés, C., Caballero, F. G., Capdevila, C. and San Martín, D., Revealing austenite grain boundaries by thermal etching: advantages and disadvantages. *Mater. Charact.*, 2003, **49**, 121–127.
38. Jones, P. T., Desmet, D., Guo, M., Durinck, D., Verhaeghe, F., Van Dyck, J., et al., High-temperature Behaviour of Magnesia–Chromite Refractories, in preparation.